Surface & Coatings Technology 475 (2023) 130159

Contents lists available at ScienceDirect

Surface & Coatings Technology

journal homepage: www.elsevier.com/locate/surfcoat

Full length article

Achieving superhydrophobicity of Zr-based metallic glass surface with anti-corrosion and anti-icing properties by nanosecond laser ablation and subsequent heat treatment

Mingming Cui [a], Hu Huang [a,*], Haoxiang Wu [a], Lin Zhang [b], Jiwang Yan [b]

[a] Key Laboratory of CNC Equipment Reliability, Ministry of Education, School of Mechanical and Aerospace Engineering, Jilin University, Changchun, Jilin 130022, China
[b] Department of Mechanical Engineering, Faculty of Science and Technology, Keio University, Yokohama 223-8522, Japan

ARTICLE INFO

Keywords:
Anti-corrosion
Anti-icing
Hierarchical micro/nanostructure
Metallic glass
Nanosecond laser
Superhydrophobic surface

ABSTRACT

Water repellency of superhydrophobic surfaces offers an opportunity to enhance the corrosion and icing resistance of metallic glasses (MGs). Inspired by the "lotus effect" in nature, hierarchical micro/nanostructures were constructed on a Zr-based MG surface using nanosecond laser ablation. By subsequent heat treatment in air, the structured surface showed a water contact angle (CA) of 168.2 ± 1.5° and a sliding angle (SA) of 4 ± 0.7° (adhesion force of 9.8 ± 1.7 μN), exhibiting repellency and low adhesion to water. Specifically, the superhydrophobic surface stored in air and immersed in water possessed stability and durability, and the superhydrophobic surface still maintained superhydrophobicity after mechanical scratching. The heat treatment temperature worked as a switch for controlling the wettability transition, and by tuning the temperature, the structured surface can switch from superhydrophobicity (CA: 168.2 ± 1.5°) to superhydrophilicity (CA: ~0°). Furthermore, compared to the polished MG surface, the superhydrophobic surface increased the corrosion resistance and freezing time, and delayed the freezing temperature. This study provides a facile non-fluorinated method for fabricating superhydrophobic MG surfaces with anti-corrosion and anti-icing properties, which would enhance the application of MGs as structural and functional materials under extreme conditions.

1. Introduction

Corrosion and icing are common natural phenomena. Metallic corrosion is inevitable due to the presence of ions and water vapor in the atmosphere [1,2], which could significantly reduce the metallic strength and destroy the metal component's geometry. In addition, Earth's metal resources are finite [3], and metal corrosion accelerates the depletion of natural resources. Meanwhile, icing is inconvenient and hazardous to human production and life [4–6]. For example, icing could increase the self-weight of the transmission line, leading to a breakdown of the entire transmission network in severe cases. Airplane wings are susceptible to icing when they encounter supercooled water droplets at high altitudes. This will affect the lift coefficient of the aircraft and may even cause a serious air crash. Hence, metallic corrosion and icing resistance are challenging issues in global production and economic construction.

The metallic glass (MG) is an emerging metal material, possessing high hardness and wear resistance, superior magnetic property and high strength compared with conventional crystalline alloys [7–11]. It has been used in sports equipment [12], medical devices [13,14], microelectromechanical systems [15,16], and space engineering [11,17]. Improving the corrosion resistance and anti-icing capability of MGs will further broaden their functional applications under extreme conditions. For example, MG materials can be applied to radar antennas. Once the surface of the antenna freezes in rainy and snowy weather conditions, it would seriously affect the performance of the radar. Therefore, it is important to improve the anti-icing performance of MG. In addition, MG materials can be applied to medical implants, so enhancing MG's corrosion resistance would significantly improve their service life. Owing to the water repellency properties and the reduced solid-liquid contact area of the superhydrophobic surface, the construction of superhydrophobic surfaces on material substrates makes it possible to achieve increased corrosion and icing resistance [18–21]. A rough microstructure and low-surface free energy are essential for achieving superhydrophobicity [22–24]. Currently, some typical methods such as

* Corresponding author.
E-mail address: huanghu@jlu.edu.cn (H. Huang).

https://doi.org/10.1016/j.surfcoat.2023.130159
Received 24 August 2023; Received in revised form 30 October 2023; Accepted 31 October 2023
Available online 2 November 2023

chemical etching [25], thermoplastic forming [26,27], and laser processing technology [28,29] have been employed to prepare micro/nanostructures on MG surfaces. Chemical etching could introduce chemical reagent, which is potentially harmful to operators and environment. Thermoplastic forming method is highly dependent on micro/nano scale template and processing temperature, and the high mold manufacturing cost as well as complex manufacturing process makes it not suitable for large scale application in engineering practice.

By comparison, nanosecond laser processing technology offers a high-efficiency, low-cost, and environmentally friendly technique for fabricating surface microstructures. As for reducing the surface free energy of micro/nanostructures, it is generally achieved by fluoroalkylsilane modification [30], low-pressure processing [31], atmospherically aged method [32], or adsorbing C–C/C–H species in the air through heat treatment [33]. Fluoroalkylsilane modification is unavoidable to have potential threats to human health and ecological environment. In addition, the low-pressure processing need a vacuum level of 10^{-6} Pa, which is not conducive to large-scale industrial adoption. The atmospherically aged method needs a few weeks, leading to low efficiency for fabricating superhydrophobic surfaces. Therefore, nanosecond laser processing combined with subsequent heat treatment would be a convenient, nontoxic, efficient, and low-cost method for preparing superhydrophobic surfaces on MG. For example, Wang et al. utilized nanosecond laser texturing and heat treatment, achieving synchronous superhydrophobicity and hardening of MG surfaces [34]. Qian et al. used this combined method to tune MG surface wettability, showing the application in directional transport of water droplets [35]. In our previous study, tunable adhesion superhydrophobic surfaces were constructed on MG through the same compounding processes, which enriched MG's applications in self-cleaning and no-loss liquid transportation [33]. However, the stability and durability of MG superhydrophobic surfaces prepared by the combined method has not been investigated. Moreover, it is still not clear whether nanosecond laser processing combined with subsequent heat treatment can enhance the corrosion resistance and icing resistance of MG based on literature review, which requires further exploration.

In this study, hierarchical micro/nanostructures were fabricated on a Zr-based MG by optimizing nanosecond laser power and scanning speed. After the adsorption of the nonpolar C–C/C–H species from air to reduce the surface free energy using heat treatment, a low-adhesion superhydrophobic surface was introduced onto the MG substrate. The superhydrophobic surface possessed stability and durability in air and water, and the contact angle (CA) of the superhydrophobic surface was larger than 150° after mechanical scratching. Furthermore, electrochemical and anti-icing tests verified the anti-corrosion and anti-icing abilities of the superhydrophobic surface. Therefore, this study provides an efficient and low-cost method for fabricating low-adhesion MG superhydrophobic surfaces without using any chemicals, which would broaden the applications of MG in anti-corrosion and anti-icing fields.

2. Experimental section

2.1. Preparation of the superhydrophobic surface

First, commercial Zr-based MG ($Zr_{41.2}Ti_{13.8}Cu_{12.5}Ni_{10}Be_{22.5}$, at.%) plates with 2 mm thickness were polished to a surface roughness S_a of approximately 10 nm, which is measured by a three-dimensional (3D) optical profiler (Zygo NewView 9000, Ametek, USA) with a resolution of sub-nanometer. The 3D optical profiler for measuring S_a, S_q, and S_z works as follows: the interference microscope measures height variations between test and reference surfaces, and then S_a, S_q, and S_z are calculated based on the interference phenomenon.

Subsequently, the polished MG plates were ablated by a nanosecond laser system (SP-050P-A-EP-*Z*-F-Y, SPI Lasers, UK) with a 1064 nm wavelength, 230 ns pulse width, and 50 kHz repetition frequency. The output power and pulse energy of the nanosecond laser system were 50 W and 0.79 mJ, respectively. The laser beam (TEM_{00} mode, $M^2 < 1.6$) had a Gaussian energy distribution. In Fig. 1, the laser beam diameter and distance between the two adjacent scanning lines were 43 and 20 μm, respectively.

The effect of the laser parameters on the surface microstructure morphology was investigated by employing different average laser powers and scanning speeds in the experiment, which corresponded to Cases 1–6 (Table 1). The peak laser power density I can be calculated by the following equation:

$$I = \frac{P_{\mathrm{avg}}}{f \times p_{\mathrm{t}} \times A_{\mathrm{lb}}} \tag{1}$$

where P_{avg} is the average laser power, f is the repetition frequency, p_{t} is the pulse width, and A_{lb} is the area of laser beam. The laser fluence a can be calculated by the following equation:

$$a = \frac{P_{\mathrm{avg}} \times t}{A_{\mathrm{lb}}} \tag{2}$$

where t is the total time. The number of pulse N means the number of laser pulses per unit laser ablation length, and N can be calculated by the following equation:

$$N = \frac{f}{v} \tag{3}$$

where v is the laser scanning speed. The existence of micro and nano-sized particles formed on the surface of metals after laser treatment would improve the superhydrophobicity of the surface, so the ablated MG plates were placed in the muffle furnace (KSL-1000X, Hefei Kejing Materials Technology Corporation, China) under the air atmosphere for heating treatment without surface cleaning after laser ablation. To achieve superhydrophobicity of the ablated MG plates, the temperature of 200 °C and time of 1 h were selected based on lots of pre-experiments.

2.2. Characterizations of the surface structures, wettability properties, and chemical compositions

After sample preparation, the micro/nanostructures and roughness S_a, S_q, and S_z of the ablated MG surfaces were characterized through field emission scanning electron microscope (FESEM, SU8010, Hitachi, Japan) and 3D optical profiler, respectively. The number of micro/nanoparticles on the laser-ablated surface was counted by the ImageJ software, and the increase or decrease of micro/nanoparticles was determined by comparing the number of micro/nanoparticles under different experimental parameters on an area of the same size. The

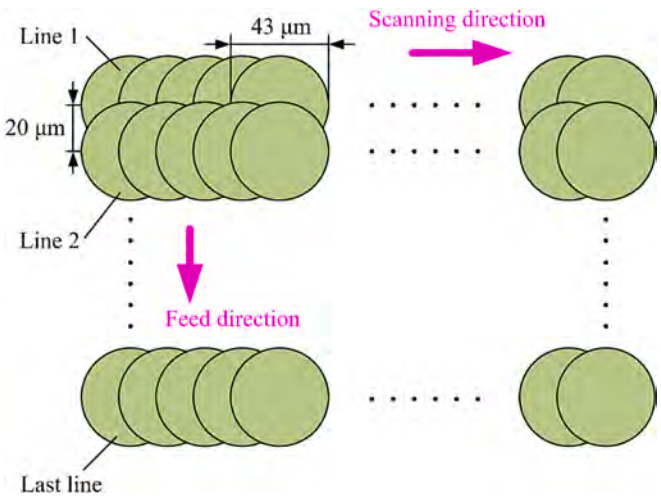

Fig. 1. Laser scanning paths corresponding to Cases 1–6.

Table 1
Laser parameters corresponding to Cases 1–6.

Case	1	2	3	4	5	6
Average laser power (W)	3.3	3.7	4.0	3.7	3.7	3.7
Peak laser power density ($\times 10^{11}$ W/m^2)	2.0	2.2	2.4	2.2	2.2	2.2
Laser influence (J/cm^2)	4.5	5.1	5.5	5.1	5.1	5.1
Scanning speed (mm/s)	10	10	10	20	50	100
Number of pulse ($\times 10^3$ mm^{-1})	5	5	5	2.5	1	0.5

wettability of the ablated MG surfaces perpendicular to laser scanning direction after heat treatment was evaluated by measuring the CA and sliding angle (SA) using a CA meter (OSA60, NBSI, China) with 5 μL water. In addition, pH = 1–14 resolutions were selected to drop on the superhydrophobic surface, and the CA and SA of the superhydrophobic surface were studied by changing with pH. The working principle of the CA measuring device was based on the analysis of a sessile drop formed on the sample surface. 8-bit grey images of the sessile drop were obtained from an orthogonal perspective (perpendicular to its rotational axis) and were processed to extract the contour coordinates of a drop silhouette based on a sub-pixel routine. These contour coordinates were then fitted to the Laplace-Young equation. From the best fitting solution, the value of CA can be obtained. The error in measuring CAs depends in principle on the perfection of the droplet: if the droplet was perfectly axis-symmetrical, the error was less than 0.3°. To compare the adhesion force of superhydrophobic surfaces, a high-speed camera (pco.dimax HS4, Excelitas PCO GmbH, Germany) was used to observe the dynamic bouncing behavior of the water droplets (diameter: 2.56 mm) on the polished and superhydrophobic surfaces, and the frame rate was 5000 fps. The initial water droplet height was 30 mm, corresponding to a 0.77 m/s impact velocity on the surface. Furthermore, in order to quantitatively compare the adhesion force of superhydrophobic surfaces, the adhesion force between the superhydrophobic surface and the water droplet (5 μL) was characterized by a surface analyzer (LSA100, LAUDA Scientific, Germany).

To evaluate the uniformity of the superhydrophobic surface, the contact angle hysteresis (CAH) of the superhydrophobic surface was measured. Furthermore, to evaluate the stability and durability of the superhydrophobic surface, the change in CA with the air storage time was investigated. In addition, the underwater stability and durability of superhydrophobic surface was conducted by a similar way reported in the previous study [36]. The superhydrophobic surface was fully immersed in the water, and it was taken out of water for the CA measurement when the immersed time was 1, 3, 5, 7, 15, and 28 days. Before the CA measurement, the superhydrophobic surface was dried by high purity argon gas (0.05 MPa) for 10 s, and after the CA measurement, it was immersed in the water again. To evaluate the resistance of the superhydrophobic surface to scratch, a scratch instrument (WS-2005, Lanzhou Institute of Chemical Physics, China) with the standard Rockwell indenter was used to prefabricate scratches on the superhydrophobic surface. The scratch load was 1 N, and the scratch intervals (*SIs*) were 0.5 and 1 mm. After prefabricating scratches, the CA of the superhydrophobic surface was measured. Furthermore, the superhydrophobic surface was subjected to anti-fouling test, and the liquid used was the muddy water of 10 wt.%. X-ray diffraction (XRD, D8 Discover, Bruker, Germany) and X-ray photoelectron spectroscopy (XPS, ESCALAB 250Xi, Thermo Fisher, USA) were utilized to detect the chemical compositions of the ablated MG surfaces.

2.3. Electrochemical and anti-icing tests

The corrosion resistance of the superhydrophobic surface was evaluated through electrochemical tests that included the polarization curves (scanning rate: 0.5 mV/s) and electrochemical impedance spectra (frequency: 10^5–10^{-2} Hz) in 3.5 wt.% NaCl solution using an electrochemical workstation (CS350, CorrTest, China) with a typical three-electrode system at 25 °C. A polished or superhydrophobic MG plate with a 1 cm^2 exposed area was used as the working electrode. A platinum plate and a saturated calomel electrode were used as the counter and reference electrodes, respectively. Before the electrochemical tests, the prepared samples were placed in 3.5 wt.% NaCl solution for 30 min to ensure the measurement stability. All electrochemical experiments were performed at least thrice to illustrate repeatability.

The anti-icing performance of the superhydrophobic surface was characterized by the freezing time and temperature using a refrigeration device, as shown in Fig. S1. Before the test, a 5 μL water droplet was dropped on the prepared samples. The sample surface temperature decreased from 25 to −20 °C at 0.15 °C/s cooling rate. The freezing time is counted as the time from when a water droplet first drops onto the specimen surface until it becomes entirely frozen. The freezing temperature is defined as the temperature of a completely frozen water droplet. Furthermore, to characterize the difficulty of deicing on the sample surface, the shear force between the frozen water droplet and the sample surface was measured by a homemade scratch tester, as shown in Fig. S2. The scratch speed was 10 mm/s, and the volume of the water droplet was 10 μL. The maximum shear force is employed to demonstrate the adhesion force between the frozen water droplet and the sample surface. During the scratch test, the temperature of the refrigeration device was always kept at −20 °C.

3. Results and discussion

3.1. Construction of the superhydrophobic surface

The realization of superhydrophobicity is inseparable from micro/nanostructures and low-surface energy [22–24]. In this study, to introduce micro/nanostructures on the MG surface, the polished sample was ablated through multiline lap laser scanning (Fig. 1). Figs. 2(a)-(i) show the FESEM morphologies of hierarchical micro/nanostructures obtained at peak laser power density = 2.0×10^{11}, 2.2×10^{11}, and 2.4×10^{11} W/m^2 (scanning speed = 10 mm/s). In Case 3 (peak laser power density = 2.4×10^{11} W/m^2, scanning speed = 10 mm/s), hierarchical micro/nanostructures are machined on the MG surface. However, severe material spheroidization and many surface holes caused by the strong interaction between the nanosecond laser and the MG [37] appear on the surface. To avoid such a severe surface ablation, further decreasing the peak laser power density to 2.2×10^{11} and 2.0×10^{11} W/m^2 at the same scanning speed. It is found that the number of micro/nanoparticles dramatically reduces in Cases 1 and 2. In conclusion, the interaction between the nanosecond laser and the MG weakens with decreasing peak laser power density. Figs. 2(b), (e), (h) and S3(a)-(i) present the FESEM morphologies of hierarchical micro/nanostructures obtained by increasing the scanning speed (peak laser power density = 2.4×10^{11} W/m^2). In Cases 2, 4, 5, and 6, the number of micro/nanoparticles gradually decreases as the scanning speed increases from 10 to 100 mm/s, which indicates that the interaction between the laser and the MG weakens with the increase in scanning speed. Furthermore, Figs. 2(j)-(l) and S3(j)-(l) show 3D topographies corresponding to Cases 1–6. The surface roughness S_a, S_q, and S_z increase in Cases 1–3 but decrease in Cases 2, 4, 5, and 6. The results further demonstrate that the laser–MG interaction is enhanced when increasing the peak laser power density, and it is weakened when increasing the scanning speed.

After preparing hierarchical micro/nanostructures on the MG surface, the ablated MG samples were placed in an oven at 200 °C for 1 h. Fig. 3(a) shows the CA of the ablated MG samples under different peak laser power densities and scanning speeds after heating treatment. The CA of the ablated MG samples increases from 131.9 ± 2.2° to 168.2 ± 1.5° when the surface roughness increases (Cases 1–3). By contrast, the CA of the ablated MG samples gradually decreases from 168.2 ± 1.5° to 126.7 ± 2.4° when the surface roughness decreases (Cases 2, 4, 5, and

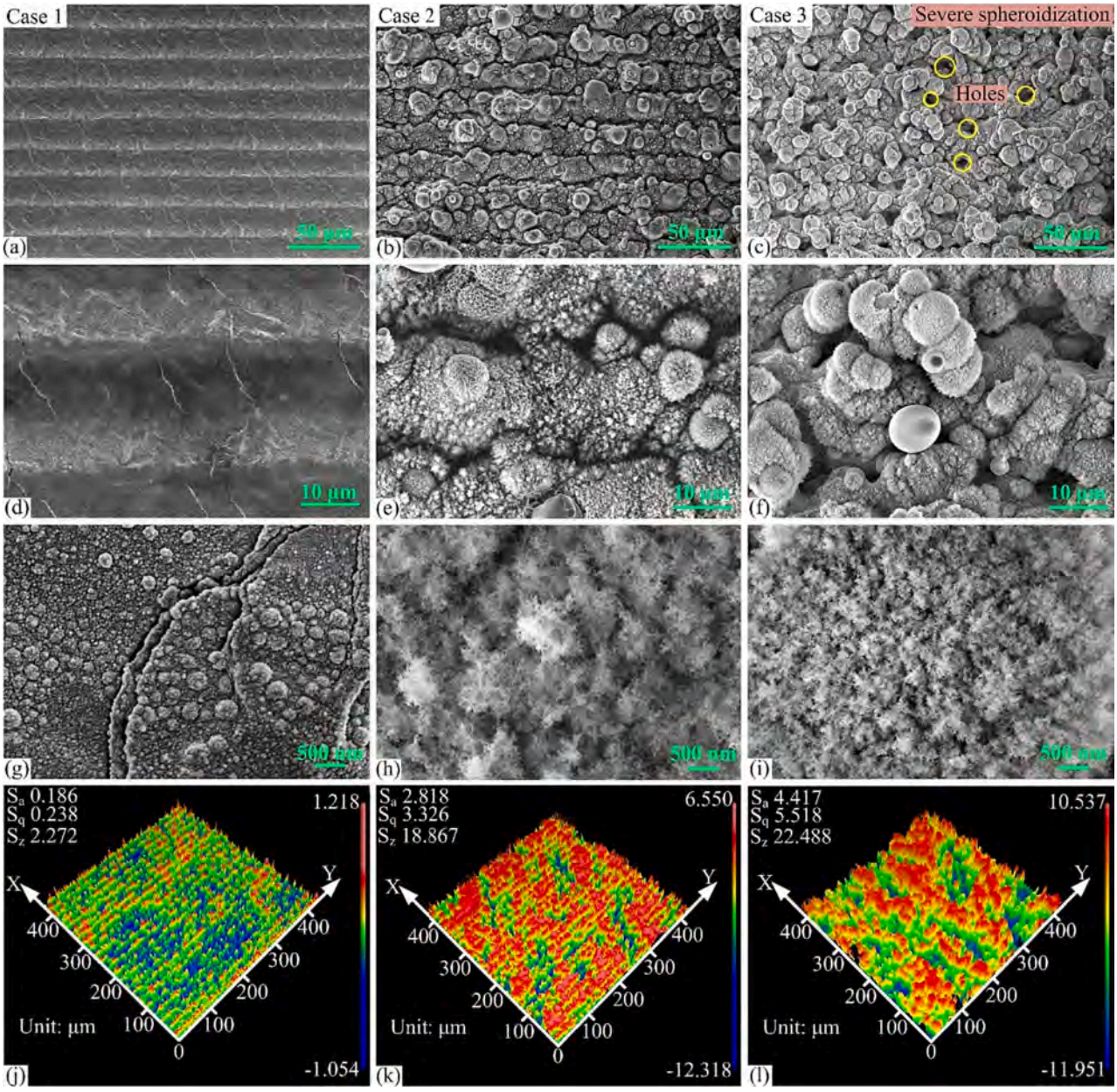

Fig. 2. FESEM morphologies of hierarchical micro/nanostructures as-prepared by laser corresponding to the laser parameters in Table 1: (a), (d), and (g) Case 1; (b), (e), and (h) Case 2; and (c), (f), and (i) Case 3. 3D topographies of hierarchical micro/nanostructures as-prepared by laser corresponding to Cases (j) 1, (k) 2, and (l) 3.

6). As the roughness of the laser-ablated surfaces for Cases 1–3 is greater than that for Cases 4–6, the contact angles of Cases 1–3 are larger than those of Cases 4–6. This confirms that hierarchical micro/nanostructures are helpful to achieve superhydrophobicity on the MG surface. Accordingly, the SA corresponding to Cases 2–4 was measured to characterize the adhesion of the superhydrophobic surface. In Fig. 3(b), the SA of the superhydrophobic surface is relatively small (4 ± 0.7°), showing low adhesion to water. This low-adhesion property was further characterized by the water droplet's bouncing behavior. As a control group, the water droplet with a 2.56 mm diameter dropped from a 30 mm height to the polished surface. The water droplet falls directly on the polished surface without bouncing up, as shown in Video S1. By comparison, the water droplet bounces 10 times on the superhydrophobic surface shown in Fig. S4. Video S2 shows more details about the dynamic bouncing behaviors of the water droplet dropping on the superhydrophobic surface. Furthermore, Fig. 3(c) presents the quantitative results of the superhydrophobic surface adhesion test, and the minimum adhesion force is only 9.8 ± 1.7 μN.

To evaluate the uniformity of the superhydrophobic surface, the CAH of superhydrophobic surface was characterized by the CA meter. Fig. 3 (d) shows the CAH of superhydrophobic surfaces, and all the CAH of superhydrophobic surfaces are less than 5°, which shows uniformity. Furthermore, the stability and durability of the superhydrophobic surface (Case 2) were investigated. As shown in Fig. 3(e), the CA of the superhydrophobic surface nearly does not change after 180 days of air storage. Moreover, the change in CA with immersion time in water is shown in Fig. 3(f), and it is still larger than 150° when the immersed time in water is 4 weeks. The results indicate that the superhydrophobic surface possesses stable and durable superhydrophobicity.

As mentioned above, the superhydrophobic surface exhibits water repellency. However, superhydrophobic surfaces cannot be immune to corrosive solutions and scratching by sharp objects under practical working conditions. First, chemical solutions with pH 1–14 were used for the CA and SA testing to further evaluate the ability of the

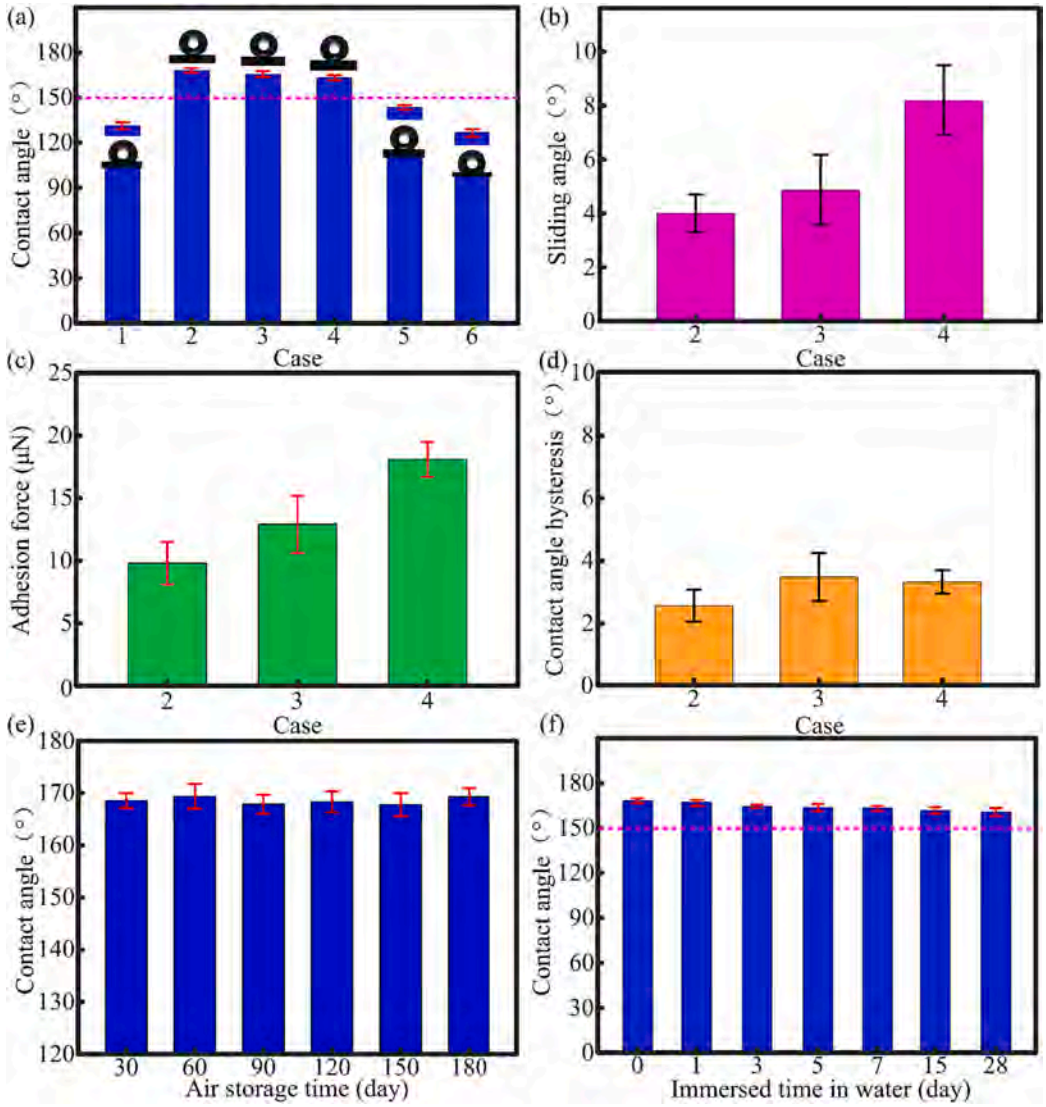

Fig. 3. (a) CA of the ablated MG samples corresponding to Cases 1–6. (b) SA, (c) adhesion force, and (d) CAH of the superhydrophobic surfaces. CA of the superhydrophobic surface changing with (e) the air storage time and (f) the immersed time in water.

superhydrophobic surface to resist the strong acid and base. Fig. 4(a) depicts that the CA and SA do not significantly change. Furthermore, crossed mechanical scratches were first introduced onto the superhydrophobic surface by mechanical scratching. The water droplets fall on the surface with a 10° inclination, as shown in Video S3. It can be seen that the water droplets easily roll off the surface, indicating that the superhydrophobic surface possesses resistance to mechanical scratches.

Fig. 4(b) shows the optical image of the water droplets with nearly spherical shapes on the superhydrophobic surface after mechanical scratching under $SI = 0.5$ and 1 mm. Furthermore, the CA of the superhydrophobic surface was measured after mechanical scratching. As shown in Fig. 4(c), the CA of the superhydrophobic surface is still larger than 150°, which demonstrates that the superhydrophobic surface after the mechanical scratching test still exhibits superhydrophobicity. In addition, the superhydrophobic surface possesses the ability to resist fouling, as shown in Video S4. Notably, the superhydrophobic surface is capable of intelligent wetting switching from superhydrophilicity to superhydrophobicity through tuning the temperature of heat treatment. As shown in Fig. 4(d), the superhydrophobic surface is transformed into a superhydrophilic surface through heat treatment at 300 °C for 1 h, and the superhydrophilic surface is converted into a superhydrophobic surface again by heating at 200 °C for 1 h. This process is defined as a complete wettability transition cycle, and the wettability transition cycle is verified by experiments of at least 10 cycles shown in Fig. S5.

3.2. Surface chemical composition

The elemental composition of surface chemistry is well known to play a crucial role in achieving superhydrophobicity. XRD and XPS were utilized herein to detect the surface chemical composition. In Fig. S6(a), the polished surface retains its amorphous character, while some crystalline phases occurr in the XRD pattern of the hierarchical micro/nanostructured surface. Based on our previous study [33], crystalline phases can be observed in metal oxides (e.g., ZrO_2, TiO_2, and CuO) and intermetallic compounds (e.g., $Cu_{10}Zr_7$ and Zr_2Cu). XPS tests were performed on the hierarchical micro/nanostructured surfaces before and after heat treatment to investigate whether the superhydrophobicity was caused by the organic substance absorption in air. Table S1 and Fig. S6(b) show the elements' content and the XPS full spectra of the hierarchical micro/nanostructured surface before and after heat treatment, and the C/Zr ratio increases from 61.96 to 238.81 after heat treatment at 200 °C for 1 h.

Furthermore, the high-resolution C 1s spectra were analyzed to verify whether the significant increase in the element C content was

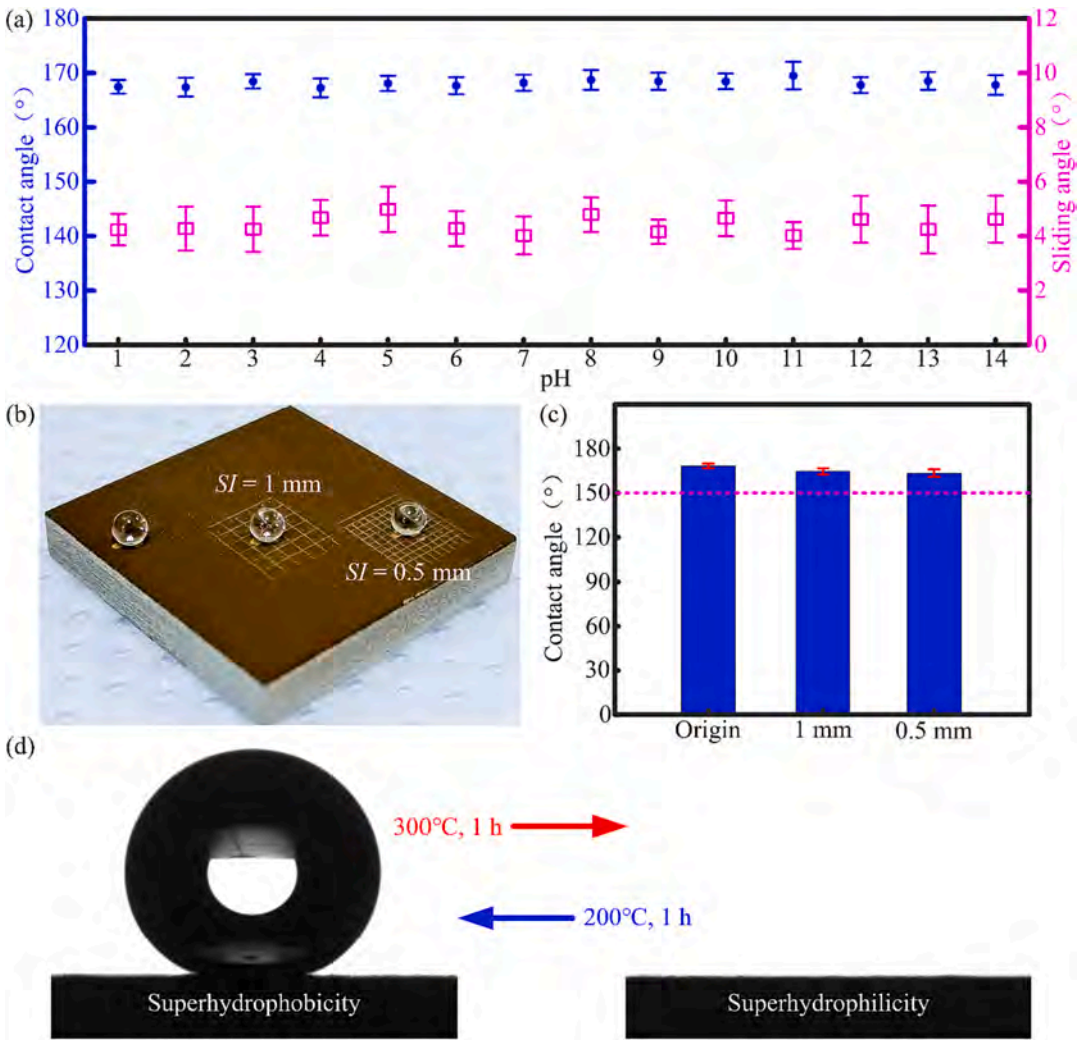

Fig. 4. (a) CA and SA of the superhydrophobic surface changing with pH. (b) Optical image of the water droplets placed on the superhydrophobic surface after the mechanical scratching test. (c) CA of the superhydrophobic surface after mechanical scratching (*SI* = 0.5 and 1 mm). (d) Intelligent wetting switching between superhydrophilicity and superhydrophobicity through tuning the temperature of heat treatment.

related to the C–C/C–H species absorption. Figs. 5(a) and (b) depict a high-resolution C 1s spectrum fitted with the three peaks of C–C/C–H at 284.8 eV, C—O at 286.3 eV, and C═O at 288.5 eV [33]. The percentage of the nonpolar C–C/C–H species increases from 75.15% to 88.51%, whereas the sum of the percentage of the polar C—O and C═O species decreases from 24.85% to 11.49%. Based on the above XPS results, Fig. 5 (d) shows the ratio of C–C/C–H corresponding to the element Zr before and after heat treatment. The ratio of C–C/C–H corresponding to the element Zr significantly increases after heat treatment at 200 °C for 1 h, indicating that the superhydrophobicity of the hierarchical micro/nanostructured surface is attributed to absorbing low-surface energy substances (C–C/C–H) from the air during heat treatment. As for the wetting transformation from superhydrophobicity to superhydrophilicity through heat treatment at 300 °C for 1 h, it may be caused by the decomposition of organic substances (C–C/C–H) at a relatively high temperature [38]. In Table S1, the C/Zr ratio decreases from 238.81 to 70.76 after heat treatment at 300 °C for 1 h. Accordingly, the percentage of the nonpolar C–C/C–H species decreases from 88.51% to 80.72%; however, the sum of the percentage of the polar C—O and C═O species increases from 11.49% to 19.28%, as shown in Figs. 5(b) and (c). Furthermore, Fig. 5(d) illustrates that the ratio of C–C/C–H species corresponding to the element Zr significantly decreases after heat treatment at 300 °C for 1 h. The results confirm that the wetting transformation from superhydrophobicity to superhydrophilicity through heat treatment at a relatively high temperature is indeed caused by the C–C/C–H species decomposition.

Based on the analysis of XPS results, the physical mechanism for the transition of wetting property with respect to temperature is shown in Fig. 5(e). The laser-ablated surface of –OH undergoes esterification with certain organic compounds containing –COOH in the air during the heating process (200 °C, 1 h), which is shown in the equation [39]:

$$\text{L-OH} + \text{R-COOH} \rightarrow \text{R-COOL} + \text{H}_2\text{O} \quad (4)$$

where L is the laser-ablated surface, and R as well as R-COOL are the alkyl species and carboxylates, respectively. During the heating treatment (200 °C, 1 h) of the laser-ablated surface, the laser-irradiated surface adsorbs a large number of nonpolar C-C/C-H species from the air, and thus its surface wettability realizes a transition from superhydrophilicity to superhydrophobicity. Furthermore, the superhydrophobic surface transforms into the superhydrophilic surface after heat treatment (300 °C, 1 h), which is attributed to the decomposition of nonpolar C-C/C-H species at relatively high temperature.

3.3. Applications of the superhydrophobic surface in anti-corrosion and anti-icing

As shown in Figs. 3(a) and (b), the hierarchical micro/

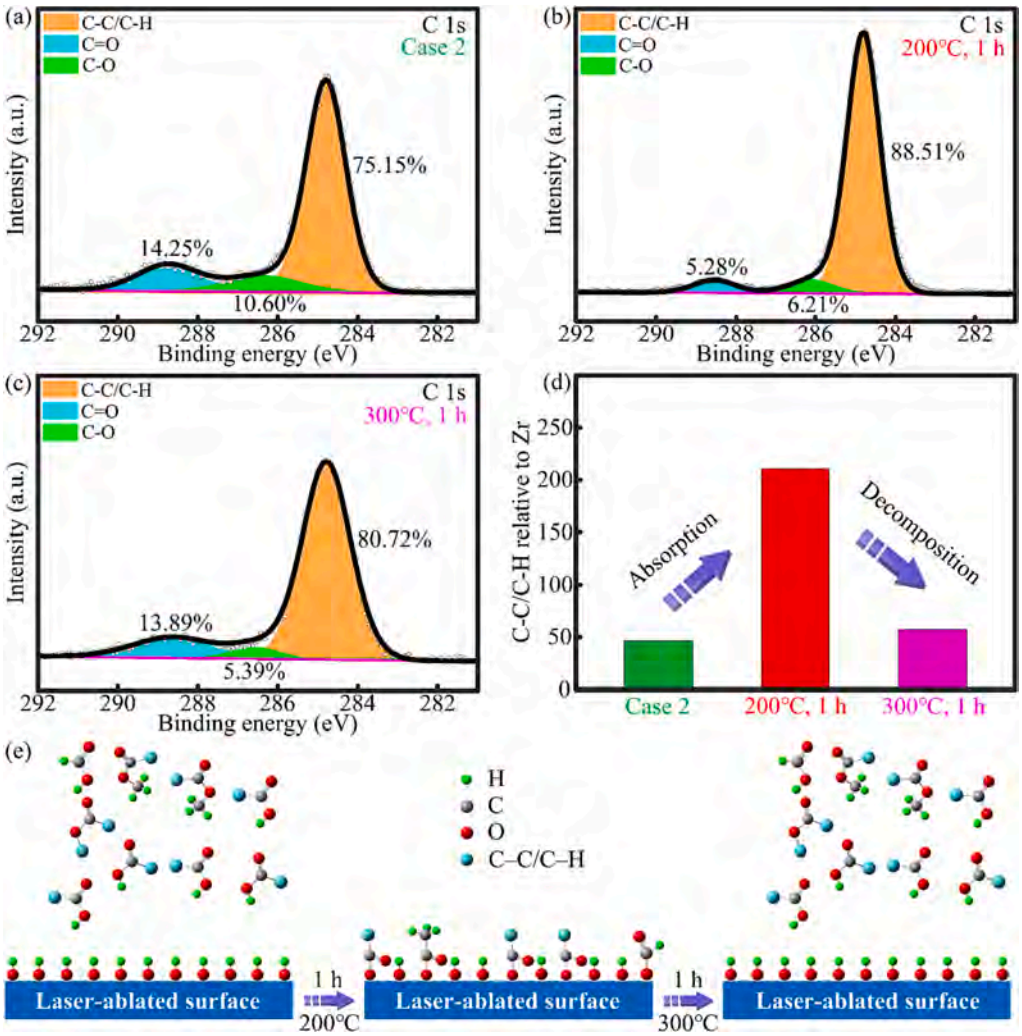

Fig. 5. High-resolution C1s corresponding to Case 2: (a) hierarchical micro/nanostructured surface, (b) hierarchical micro/nanostructured surface after heat treatment at 200 °C for 1 h. (c) Superhydrophobic surface after heat treatment at 300 °C for 1 h. (d) Ratio of C–C/C–H species relative to Zr element. (e) Physical mechanism for the transition of wetting property with respect to temperature.

nanostructured surface corresponding to Case 2 possesses a relatively large CA of 168.2 ± 1.5° and small SA of 4 ± 0.7°, depicting lower solid-liquid contact fraction and surface adhesion. Previous studies [18,40,41] have shown that introducing superhydrophobic surfaces with lower solid-liquid contact fraction and surface adhesion can enhance a material's corrosion and icing resistance. Therefore, the superhydrophobic MG samples were employed to investigate the anti-corrosion and anti-icing properties. The polarization curves and electrochemical impedance spectra are common methods for characterizing the corrosion resistance of materials. In the polarization curves, the corrosion resistance of materials is usually compared using corrosion potential E_{corr} and corrosion current density i_{corr}. A material possessing higher E_{corr} and lower i_{corr} is generally more corrosion-resistant [40,42,43].

Fig. 6(a) shows the polarization curves of the polished and superhydrophobic surfaces. Accordingly, Table 2 displays the E_{corr}, i_{corr}, anodic Tafel slope β_a, and cathodic Tafel slope β_c obtained from the method of Tafel extrapolation. Compared with the polished surface, the E_{corr} of the superhydrophobic surface increases from −231 ± 35 to −123 ± 24 mV; however, the i_{corr} of the superhydrophobic surface decreases from $(3.25 \pm 0.29) \times 10^{-6}$ to $(1.06 \pm 0.13) \times 10^{-7}$ A/cm^2. The results indicate that the corrosion resistance of MG has been improved by introducing a superhydrophobic surface on MG. Furthermore, to evaluate the protection efficiency η of the superhydrophobic surface compared with the polished surface, the polarization resistance R_P is calculated first using the following equation [44]:

$$R_P = \frac{\beta_a \times \beta_c}{2.303 \times i_{corr} \times (\beta_a + \beta_c) \times A_{ea}} \quad (5)$$

where A_{ea} is the exposed area of the working electrode (the polished or superhydrophobic surface), which is 1 cm^2 in this study. Then the η is calculated as follows [45]:

$$\eta = \frac{R_{PS} - R_{PP}}{R_{PS}} \quad (6)$$

where R_{PS} and R_{PP} are the polarization resistances of the superhydrophobic and polished surfaces, respectively. The calculated result of the η is about 0.8178, indicating that MG's corrosion resistance has been enhanced by approximately 81.78% by introducing the superhydrophobic surface. Furthermore, the difference between the polished surface and the superhydrophobic surface after electrochemical polarization curve testing is characterized. As shown in Figs. S7(a) and (b), it is obvious that the galvanic corrosion appears on the polished surface after the electrochemical corrosion test. Figs. S7(c) and (d) show the morphology of the superhydrophobic surface after electrochemical corrosion test, and the superhydrophobic surface basically maintains its

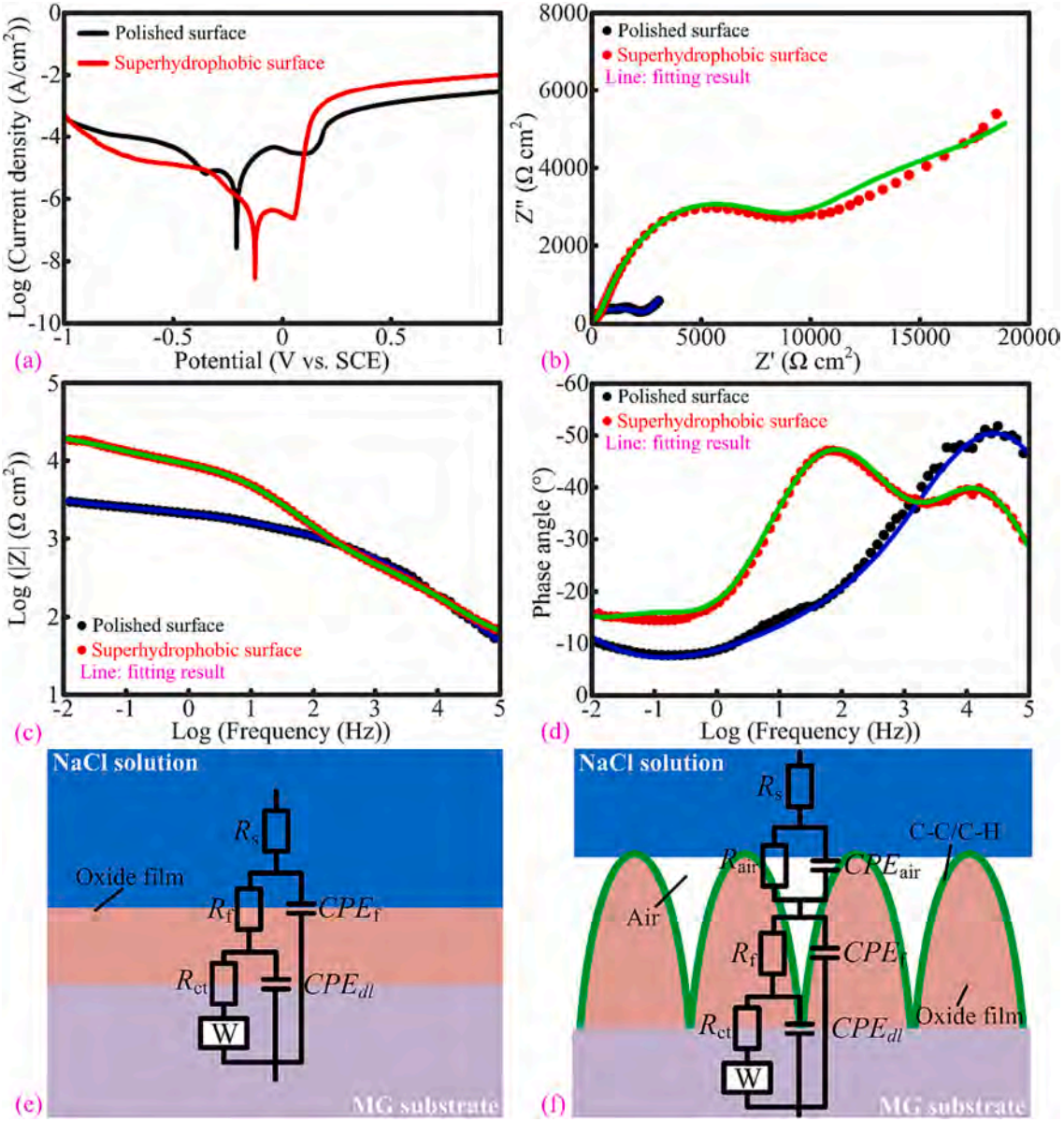

Fig. 6. (a) Polarization, (b) Nyquist, (c) impedance modulus, and (d) phase angle curves of the polished and superhydrophobic surfaces. Equivalent circuit model: (e) the polished surface and (f) the superhydrophobic surface.

Table 2
Electrochemical parameters corresponding to the polarization curves of the polished and superhydrophobic surfaces.

	Polished surface	Superhydrophobic surface (Case 2)
E_{corr} (mV)	-231 ± 35	-123 ± 24
i_{corr} (A/cm^2)	$(3.25 \pm 0.29) \times 10^{-6}$	$(1.06 \pm 0.13) \times 10^{-7}$
β_a (mV/dec)	87 ± 18	31 ± 12
β_c (mV/dec)	-118 ± 14	-65 ± 23

original morphology. The experimental results indicate that the superhydrophobic surface can effectively prevent corrosion solutions from invading the material.

The polished and superhydrophobic surfaces were characterized by the electrochemical impedance spectra to further investigate the corrosion resistance of MG when a superhydrophobic surface was introduced. The electrochemical impedance spectra include the Nyquist plot and Bode plots of the impedance and phase angle. As shown in Fig. 6 (b), the Nyquist curves of the polished and superhydrophobic surfaces both include a capacitive arc and a Warburg impedance line. The capacitive arc radius at the high-frequency region is relevant to the charger transfer process, and the Warburg impedance line at the low-frequency region corresponds to the mass transfer of the corrosion ions through the sample surface. The large capacitive arc radius of the Nyquist curve generally represents the improved corrosion resistance of the material [46,47]. The capacitive arc radius at the high-frequency region of the superhydrophobic surface is much larger than that of the polished surface, indicating that the corrosion resistance of MG is greatly improved by the introduced superhydrophobic surface. The impedance modulus and the phase angle were also analyzed to evaluate the corrosion resistance of the superhydrophobic surface. According to previous studies [48,49], a higher value of the impedance modulus at the low-frequency region meant a better corrosion resistance of the material. As shown in Fig. 6(c), the impedance modulus at the low-frequency region of the superhydrophobic surface is enhanced by approximately one magnitude compared with that of the polished surface. This confirms that the corrosion resistance of MG is enhanced by the introduction of the superhydrophobic surface. In addition, the

superhydrophobic surface possesses a new time constant at the middle-frequency region compared with the polished surface shown in Fig. 6(d), which demonstrates the corrosion resistance of the MG has been improved by introducing the superhydrophobic surface [50,51].

Furthermore, the equivalent circuit models in Figs. 6(e) and (f) are employed to fit the electrochemical impedance spectra of the polished and superhydrophobic surfaces. In Fig. 6(e), *Rs*, R_f, R_{ct}, and *W* are the resistance of the solution, oxide film, charge transfer, and Warburg impedance, respectively. CPE_f and CPE_{dl} represent the capacitance of the oxide film and electric double layer, respectively. Considering the existence of air pockets at the solid-liquid interface on the superhydrophobic surface [52], the equivalent circuit model of the superhydrophobic surface exists extra air resistance R_{air} and air capacitance CPE_{air} compared with the equivalent circuit model of the polished surface, as shown in Fig. 6(f).

Table 3 summarizes the simulation results of the electrochemical parameters based on the equivalent circuit models of the polished and superhydrophobic surfaces. According to previous studies [53,54], the higher the resistance of charge transfer R_{ct}, the lower the charge transfer rate at the metal interface. Therefore, a larger R_{ct} represents a better corrosion resistance of the material. As shown in Table 3, the R_{ct} of the superhydrophobic surface is 1.157×10^4 Ω cm^2, which is much larger than that of the polished surface (2.251×10^3 Ω cm^2). This result demonstrates that the corrosion of MG is effectively enhanced by introducing the superhydrophobic surface. The improved corrosion resistance of MG can be attributed to the formation of hierarchical micro/nanostructures with low-surface energy substances (C–C/C–H) on the MG surface, which can capture air to prevent the intrusion of corrosive solutions into the MG substrate.

The icing resistance of MG is usually evaluated using the freezing time and temperature [55,56]. A 5 μL water droplet was dropped on the polished and superhydrophobic surfaces, and then the temperature of the cooling plate decreased from 25 to −20 °C at a 0.15 °C/s cooling rate. The heat of the water droplets is mainly transferred into the samples as the temperature of the sample surface decreased, consequently leading to the freezing of water droplets. Figs. 7(a)-(h) show the dynamic processes of the water droplet freezing on the polished and superhydrophobic surfaces. As shown in Figs. 7(a)-(d) and Video S5, the water droplet starts to freeze on the polished surface at 167 s under 0 °C and becomes wholly frozen at 179 s under −1.8 °C. On the contrary, the water droplet on the superhydrophobic surface does not start to freeze until 264 s under −14.6 °C. The water droplet utterly freezes at 285 s under −17.8 °C shown in Figs. 7(e)-(h) and Video S6.

The freezing time is increased from 179 to 285 s, and the freezing temperature of the water droplet on the MG is decreased from −1.8 to −17.8 °C through the superhydrophobic surface fabrication, which can be explained by heat conduction [57] and the classical nucleation theory [58]. With reference to the heat conduction theory [57], the air trapped in the hierarchical micro/nanostructures can prevent heat exchange between the liquid droplets and low-temperature sample surfaces. Therefore, the freezing time is increased and the freezing temperature is delayed. On the other hand, from the perspective of the classical nucleation theory [58]:

$$J = J_0 exp\left(-\frac{\Delta G}{kT}\right) \tag{7}$$

where *J* is the nucleation rate of the water droplet on the sample surface, J_0 is the kinetic constant, ΔG is the free energy barrier, *k* is the Boltzmann constant, and *T* is the ambient temperature of the water droplet. Compared to the polished surface, the superhydrophobic surface with a relatively small actual solid-liquid contact area can enhance the free energy barrier between the water droplet and the sample surface, consequently slowing down the heat exchange and delaying the water freezing process. The slowdown of the nucleation rate is macroscopically manifested by the increased freezing time and the delayed freezing temperature in the experiment. Therefore, the construction of a superhydrophobic surface on MG is beneficial to enhance MG's icing resistance.

Furthermore, to investigate the difference of deicing on the superhydrophobic surface and the polished surface, the adhesion force between the frozen water droplet and the sample surface was characterized. As shown in Fig. 7(j), the adhesion force between the frozen water droplet and the superhydrophobic surface is 8.92 N, which is much smaller than that of the adhesion force between the frozen water droplet and the polished surface (see Fig. 7(i)). The results indicate that the introduction of superhydrophobic surface on the MG matrix is more conducive to deicing.

Table 3
Electrochemical parameters based on the simulation of the electrochemical impedance spectra of the polished and superhydrophobic surfaces. *R* and *W* are expressed in Ω cm^2 unit. $CPE \sim Y$ is expressed in Ω^{-1} S^n cm^{-2} unit.

Electrochemical parameter	Polished surface	Superhydrophobic surface
R_s	13.65	39.46
$CPE_{air} \sim Y$	/	2.430×10^{-6}
$CPE_{air} \sim n$	/	0. 6962
R_{air}	/	5.176×10^2
$CPE_f \sim Y$	1.802×10^{-6}	5.655×10^{-6}
$CPE_f \sim n$	0.7116	0.7103
R_f	5.107×10^2	8.974×10^3
$CPE_{dl} \sim Y$	1.112×10^{-4}	1.794×10^{-4}
$CPE_{dl} \sim n$	0.3415	0.6116
R_{ct}	2.251×10^3	1.157×10^4
W	4.925×10^{-3}	8.150×10^{-4}

4. Conclusions

In this study, superhydrophobic surfaces were introduced on a Zr-based MG substrate by combining nanosecond laser fabrication and heat treatment. After analyzing the surface structures, wettability properties, chemical compositions, and electrochemical and anti-icing testing results, the main conclusions could be drawn as follows:

(1) A superhydrophobic surface with a relatively large CA (168.2 ± 1.5°) and small SA (4 ± 0.7°) was prepared on the Zr-based MG substrate.
(2) The superhydrophobic surface possessed low-adhesion force to the water droplet (9.8 ± 1.7 μN) and showed stability and durability in both air and water for extended periods of time.
(3) After mechanical scratching under the load of 1 N (*SI* = 0.5 and 1 mm), the superhydrophobic surface still exhibited superhydrophobicity.
(4) The hierarchical micro/nanostructured surface showed intelligent wetting switching between superhydrophilicity and superhydrophobicity by tuning the temperature of heat treatment, corresponding to the decomposition (300 °C) and absorption (200 °C) of C–C/C–H species.
(5) Via introducing a superhydrophobic surface on the MG substrate, MG's corrosion resistance was enhanced by about 81.78%, and the charge-transfer impedance increased from 2.251×10^3 to 1.157×10^4 Ω cm^2; the improved resistance to icing of MG was reflected in the increased freezing time from 179 to 285 s and decreased freezing temperature from −1.8 to −17.8 °C, and the adhesion force decreased from 19.33 to 8.92 N.

Supplementary data to this article can be found online at https://doi.org/10.1016/j.surfcoat.2023.130159.

CRediT authorship contribution statement

Mingming Cui: Investigation, Formal analysis, Data curation, Writing – original draft. **Hu Huang:** Conceptualization, Funding

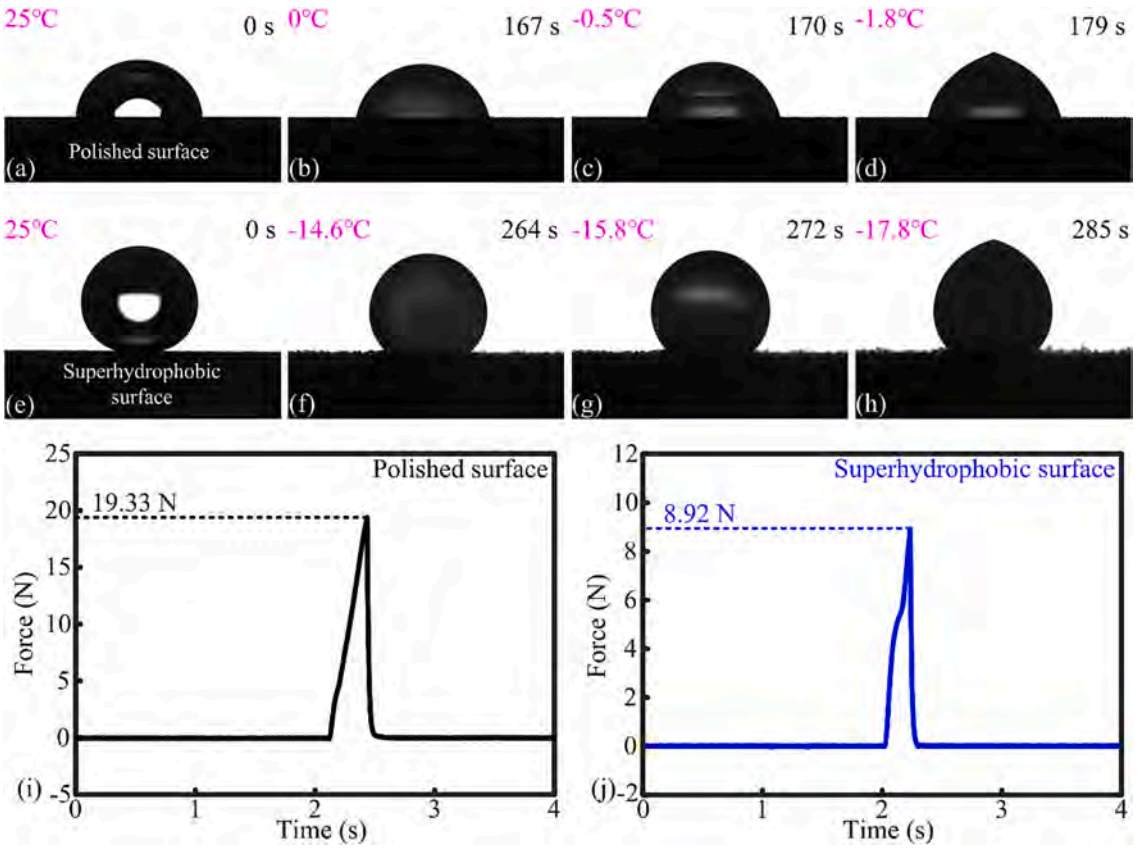

Fig. 7. Dynamic processes of the water droplet frozen on (a)-(d) the polished surface and (e)-(h) the superhydrophobic surface. Force between the frozen water droplet and the sample surface: (i) the polished surface and (j) the superhydrophobic surface.

acquisition, Methodology, Resources, Supervision, Writing – review & editing. **Haoxiang Wu:** Investigation, Validation. **Lin Zhang:** Investigation. **Jiwang Yan:** Supervision.

Declaration of competing interest

The authors declare that they have no known competing financial interests or personal relationships that could have appeared to influence the work reported in this paper.

Data availability

Data will be made available on request.

Acknowledgements

This work was supported by the Natural Science Foundation of Jilin Province (20220101198JC), the National Key Research and Development Plan Project (Grant No. 2022YFB4600204), the Graduate Innovation Fund of Jilin University (Grant No. 2023CX062), the Opening Project of the Key Laboratory of CNC Equipment Reliability, Ministry of Education, Jilin University (JLU-cncr-202306), and the Fundamental Research Funds for the Central Universities (2023-JCXK-02).

References

[1] D. Zang, R. Zhu, W. Zhang, X. Yu, L. Lin, X. Guo, M. Liu, L. Jiang, Corrosion-resistant superhydrophobic coatings on Mg alloy surfaces inspired by lotus seedpod, Adv. Funct. Mater. 27 (8) (2017) 1–7.
[2] Z. Qiu, Z. Li, H. Fu, H. Zhang, Z. Zhu, A. Wang, H. Li, L. Zhang, H. Zhang, Corrosion mechanisms of Zr-based bulk metallic glass in NaF and NaCl solutions, J. Mater. Sci. Technol. 46 (2020) 33–43.
[3] S.M. Jowitt, G.M. Mudd, J.F.H. Thompson, Future availability of non-renewable metal resources and the influence of environmental, social, and governance conflicts on metal production, Commun. Earth Environ. 1 (2020) 13.
[4] P. Wang, T. Yao, Z. Li, W. Wei, Q. Xie, W. Duan, H. Han, A superhydrophobic/electrothermal synergistically anti-icing strategy based on graphene composite, Compos. Sci. Technol. 198 (2020), 108307.
[5] L. Wang, Z. Tian, G. Jiang, X. Luo, C. Chen, X. Hu, H. Zhang, M. Zhong, Spontaneous dewetting transitions of droplets during icing & melting cycle, Nat. Commun. 13 (2022) 378.
[6] Z. He, C. Wu, M. Hua, S. Wu, D. Wu, X. Zhu, J. Wang, X. He, Bioinspired multifunctional anti-icing hydrogel, Matter 2 (3) (2020) 723–734.
[7] J. Hong, Y. Qian, L. Zhang, H. Huang, M. Jiang, J. Yan, Laser nitriding of Zr-based metallic glass: an investigation by orthogonal experiments, Surf. Coat. Technol. 424 (2021), 127657.
[8] L. Ward, S.C. O'Keeffe, J. Stevick, G.R. Jelbert, M. Aykol, C. Wolverton, A machine learning approach for engineering bulk metallic glass alloys, Acta Mater. 159 (2018) 102–111.
[9] M.M. Khan, I. Shabib, W. Haider, A combinatorially developed Zr-Ti-Fe-Al metallic glass with outstanding corrosion resistance for implantable medical devices, Scr. Mater. 162 (2019) 223–229.
[10] P. Tiberto, M. Baricco, E. Olivetti, R. Piccin, Magnetic properties of bulk metallic glasses, Adv. Eng. Mater. 9 (6) (2007) 468–474.
[11] A.G. Murphy, P. Meagher, A. Norman, D.J. Browne, Mechanical and thermal stability of bulk metallic glass alloys identified as candidates for space mechanism applications, Mater. Des. 224 (2022), 111350.
[12] N.W. Khun, H. Yu, Z.Z. Chong, P. Tian, Y. Tian, S.B. Tor, E. Liu, Mechanical and tribological properties of Zr-based bulk metallic glass for sports applications, Mater. Des. 92 (2016) 667–673.
[13] P. Meagher, E.D. O'Cearbhaill, J.H. Byrne, D.J. Browne, Bulk metallic glasses for implantable medical devices and surgical tools, Adv. Mater. 28 (27) (2016) 5755–5762.
[14] M. Cihova, E. Müller, Y. Chandorkar, K. Thorwarth, G. Fortunato, K. Maniura-Weber, J.F. Löffler, M. Rottmar, Palladium-based metallic glass with high thrombogenic resistance for blood-contacting medical devices, Adv. Funct. Mater. 32 (4) (2021) 2108256.
[15] M. Gao, J.H. Perepezko, Al-based amorphous metallic plastics, Adv. Eng. Mater. 21 (4) (2019), 1800930.
[16] J. Li, C. Li, S. Wang, H. Wang, S. Kou, Thermal processing map and thermoplastic forming map of Zr-based bulk metallic glass in the supercooled liquid region, J. Non-Cryst. Solids 570 (2021), 121008.

[17] C. Liao, M. Liu, Q. Zhang, W. Dong, R. Zhao, B. Li, Z. Jiao, J. Song, W. Yao, S. Zhao, H. Bai, W.H. Wang, Low-temperature thermoplastic welding of metallic glass ribbons for in-space manufacturing, Sci. China Mater. 64 (4) (2020) 979–986.
[18] J. Zang, S. Yu, G. Zhu, X. Zhou, Fabrication of superhydrophobic surface on aluminum alloy 6061 by a facile and effective anodic oxidation method, Surf. Coat. Technol. 380 (2019), 125078.
[19] Y. Ye, Z. Kang, F. Wang, Y. Long, T. Guo, D. Chen, J. Kong, L. Xu, Achieving hierarchical structure with superhydrophobicity and enhanced anti-corrosion via electrochemical etching and chemical vapor deposition, Appl. Surf. Sci. 610 (2023), 155362.
[20] X. Li, G. Wang, A.S. Moita, C. Zhang, S. Wang, Y. Liu, Fabrication of bio-inspired non-fluorinated superhydrophobic surfaces with anti-icing property and its wettability transformation analysis, Appl. Surf. Sci. 505 (2020), 144386.
[21] H. Zheng, S. Chang, Y. Zhao, Anti-icing & icephobic mechanism and applications of superhydrophobic/ultra slippery surface, Prog. Chem. 29 (1) (2017) 102–118.
[22] Y. Shu, X. Lu, Y. Liang, W. Su, W. Gao, J. Yao, Z. Niu, Y. Lin, Y. Xie, Nanosecond laser fabrication of superhydrophobic copper and anti-frost surface on copper, Surf. Coat. Technol. 441 (2022), 128514.
[23] G.V. Kuznetsov, D.V. Feoktistov, E.G. Orlova, K. Batishcheva, S.S. Ilenok, Unification of the textures formed on aluminum after laser treatment, Appl. Surf. Sci. 469 (1) (2019) 974–982.
[24] N.X. Zhu, Z.W. Wei, C.X. Chen, D. Wang, C.C. Cao, Q.F. Qiu, J.J. Jiang, H.P. Wang, C.Y. Su, Self-generation of surface roughness by low-surface-energy alkyl chains for highly stable superhydrophobic/superoleophilic MOFs with multiple functionalities, Angew. Chem. Int. Ed. Eng. 58 (47) (2019) 17033–17040.
[25] K. Liu, Z. Li, W. Wang, L. Jiang, Facile creation of bio-inspired superhydrophobic Ce-based metallic glass surfaces, Appl. Phys. Lett. 99 (26) (2011), 261905.
[26] N. Li, W. Chen, L. Liu, Thermoplastic micro-forming of bulk metallic glasses: a review, Jom 68 (4) (2016) 1246–1261.
[27] N. Li, J. Pan, Z. Liu, L. Liu, Metallic glass nanostructures: forming strategies and functional applications, Mater. Today Adv. 15 (2022), 100253.
[28] J. Wang, P. Zhang, L. Shen, Z. Yu, H. Shi, Y. Tian, The femtosecond laser induced $Zr_{64.13}Cu_{15.75}Ni_{10.12}Al_{10}$ amorphous periodic surface structure, J. Manuf. Process. 69 (2021) 613–620.
[29] M. Cui, H. Huang, L. Zhang, J. Yan, Nanosecond laser “pulling” patterning of micro–nano structures on Zr-based metallic glass, Small 19 (14) (2023) 2206516.
[30] Y. Qian, M. Jiang, Z. Zhang, H. Huang, J. Yan, On the transformation between micro-concave and micro-convex in nanosecond laser ablation of a Zr-based metallic glass, J. Manuf. Process. 68 (2021) 1114–1122.
[31] J. Radhakrishnan, M. Diaz, F. Cordovilla, J.L. Ocaña, Tunable superhydrophobic titanium nitride surface by ultrafast laser processing, Ceram. Int. 48 (24) (2022) 37264–37274.
[32] J. Radhakrishnan, M. Diaz, F. Cordovilla, J. Kopecek, J.L. Ocaña, Water droplets impact dynamics on laser engineered superhydrophobic ceramic surface, Opt. Laser Technol. 158 (2023), 108887.
[33] M. Cui, H. Huang, C. Wang, L. Zhang, J. Yan, Achieving superhydrophobicity of Zr-based metallic glass surfaces with tunable adhesion by nanosecond laser ablation and annealing, ACS Appl. Mater. Interfaces 14 (34) (2022) 39567–39576.
[34] Q.H. Wang, Y.Y. Cheng, Z.X. Zhu, N. Xiang, H.X. Wang, Modulation and control of wettability and hardness of Zr-based metallic glass via facile laser surface texturing, Micromachines 12 (11) (2021) 1322.
[35] Y. Qian, H. Liu, L. Zhang, M. Jiang, H. Huang, J. Yan, Tailoring the surface characteristic of metallic glass for wettability control, J. Mater. Res. Technol. 24 (2023) 7040–7046.
[36] A.Y. Zhizhchenko, A.V. Shabalina, A.A. Aljulaih, S.O. Gurbatov, A.A. Kuchmizhak, S. Iwamori, S.A. Kulinich, Stability of octadecyltrimethoxysilane-based coatings on aluminum alloy surface, Materials 15 (5) (2022) 1804.
[37] H. Huang, J. Yan, Surface patterning of Zr-based metallic glass by laser irradiation induced selective thermoplastic extrusion in nitrogen gas, J. Micromech. Microeng. 27 (7) (2017), 075007.
[38] X.Y. Li, Y. Jiang, Z.H. Jiang, Y.C. Li, C.E. Wen, J.S. Lian, Reversible wettability transition between superhydrophilicity and superhydrophobicity through alternate heating-reheating cycle on laser-ablated brass surface, Appl. Surf. Sci. 492 (2019) 349–361.
[39] R. Jagdheesh, M. Diaz, S. Marimuthu, J.L. Ocana, Robust fabrication of μ-patterns with tunable and durable wetting properties: hydrophilic to ultrahydrophobic via a vacuum process, J. Mater. Chem. A 5 (15) (2017) 7125–7136.
[40] W. Yao, W. Liang, G. Huang, B. Jiang, A. Atrens, F. Pan, Superhydrophobic coatings for corrosion protection of magnesium alloys, J. Mater. Sci. Technol. 52 (2020) 100–118.
[41] T. Hao, Z. Zhu, H. Yang, Z. He, J. Wang, All-day anti-icing/deicing film based on combined photo-electro-thermal conversion, ACS Appl. Mater. Interfaces 13 (37) (2021) 44948–44955.
[42] A. Mehrvarz, Y. Ghazanfar-Ahari, J. Khalil-Allafi, S. Mahdavi, M. Etminanfar, The microstructural features and corrosion behavior of hydroxyapatite/ZnO nanocomposite electrodeposit on NiTi alloy: effect of current density, Ceram. Int. 48 (2) (2022) 2191–2202.
[43] M.S. Safavi, M. Fathi, I. Ahadzadeh, Feasible strategies for promoting the mechano-corrosion performance of Ni-Co based coatings: which one is better? Surf. Coat. Technol. 420 (2021), 127337.
[44] M. Stern, A.L. Geary, Electrochemical polarization, J. Electrochem. Soc. 104 (1) (1957) 56–63.
[45] U. Trdan, T. Sano, D. Klobčar, Y. Sano, J. Grum, R. Šturm, Improvement of corrosion resistance of AA2024-T3 using femtosecond laser peening without protective and confining medium, Corros. Sci. 143 (2018) 46–55.
[46] H. Chen, H. Fan, N. Su, R. Hong, X. Lu, Highly hydrophobic polyaniline nanoparticles for anti-corrosion epoxy coatings, Chem. Eng. J. 420 (2021), 130540.
[47] H. Seifiyan, M. Heydarzadeh Sohi, M. Ansari, D. Ahmadkhaniha, M. Saremi, Influence of friction stir processing conditions on corrosion behavior of AZ31B magnesium alloy, J. Magnes. Alloy 7 (4) (2019) 605–616.
[48] A.C. Balaskas, T. Hashimoto, M. Curioni, G.E. Thompson, Two-shell structured PMAA@CeO2 nanocontainers loaded with 2-mercaptobenzothiazole for corrosion protection of damaged epoxy coated AA 2024-T3, Nanoscale 9 (17) (2017) 5499–5508.
[49] M. Saveleva, A. Vladescu, C. Cotrut, L. Van der Meeren, M. Surmeneva, R. Surmenev, B. Parakhonskiy, A.G. Skirtach, The effect of hybrid coatings based on hydrogel, biopolymer and inorganic components on the corrosion behavior of titanium bone implants, J. Mater. Chem. B 7 (43) (2019) 6778–6788.
[50] Y. Liu, J. Zhang, S. Li, Y. Wang, Z. Han, L. Ren, Fabrication of a superhydrophobic graphene surface with excellent mechanical abrasion and corrosion resistance on an aluminum alloy substrate, RSC Adv. 4 (85) (2014) 45389–45396.
[51] W. Liu, Q. Xu, J. Han, X. Chen, Y. Min, A novel combination approach for the preparation of superhydrophobic surface on copper and the consequent corrosion resistance, Corros. Sci. 110 (2016) 105–113.
[52] J.Y. Long, P.X. Fan, D.W. Gong, D.F. Jiang, H.J. Zhang, L. Li, M.L. Zhong, Superhydrophobic surfaces fabricated by femtosecond laser with tunable water adhesion: from lotus leaf to rose petal, ACS Appl. Mater. Interfaces 7 (18) (2015) 9858–9865.
[53] Y. Wan, M. Chen, W. Liu, X. Shen, Y. Min, Q. Xu, The research on preparation of superhydrophobic surfaces of pure copper by hydrothermal method and its corrosion resistance, Electrochim. Acta 270 (2018) 310–318.
[54] Y. Chen, Y.W. Liu, Y. Xie, H.H. Zhang, Z. Zhang, Preparation and anti-corrosion performance of superhydrophobic silane/graphene oxide composite coating on copper, Surf. Coat. Technol. 423 (2021), 127622.
[55] M. Fenero, M. Knez, I. Saric, M. Petravic, H. Grande, J. Palenzuela, Omniphobic etched aluminum surfaces with anti-icing ability, Langmuir 36 (37) (2020) 10916–10922.
[56] S. Zhang, J. Huang, Y. Cheng, H. Yang, Z. Chen, Y. Lai, Bioinspired surfaces with superwettability for anti-icing and ice-phobic application: concept, mechanism, and design, Small 13 (48) (2017) 1701867.
[57] W. Li, Y. Zhan, S. Yu, Applications of superhydrophobic coatings in anti-icing: theory, mechanisms, impact factors, challenges and perspectives, Prog. Org. Coat. 152 (2021), 106117.
[58] N.H. Fletcher, Size effect in heterogeneous nucleation, J. Chem. Phys. 29 (3) (1958) 572–576.